High-resolution ALMA observations of H2S in LIRGs: Dense gas and shocks in outflows and circumnuclear disks

(article starts on next page)

Astronomy & Astrophysics

High-resolution ALMA observations of H₂S in LIRGs

Dense gas and shocks in outflows and circumnuclear disks

M. T. Sato[1],[*] , S. Aalto[1] , S. König[2] , K. Kohno[3] , S. Viti[4,5,6] , M. Gorski[7] , F. Combes[8] , S. García-Burillo[9] ,
N. Harada[10] , P. van der Werf[4] , J. Otter[11] , S. Muller[1] , Y. Nishimura[3] , J. S. Gallagher[12] , A. S. Evans[13,14] ,
K. M. Dasyra[15] , and J. K. Kotilainen[16]

[1] Department of Space, Earth & Environment, Chalmers University of Technology, SE-412 96 Gothenburg, Sweden
[2] Department of Space, Earth and Environment, Onsala Space Observatory, Chalmers University of Technology, SE-439 92 Onsala, Sweden
[3] Institute of Astronomy, The University of Tokyo, 2-21-1 Osawa, Mitaka, Tokyo 181-0015, Japan
[4] Leiden Observatory, Leiden University, PO Box 9513, NL-2300 RA Leiden, The Netherlands
[5] Transdisciplinary Research Area (TRA) 'Matter'/Argelander-Institut für Astronomie, University of Bonn, Bonn, Germany
[6] Physics and Astronomy, University College London, London, UK
[7] Center for Interdisciplinary Exploration and Research in Astrophysics (CIERA) Northwestern University, Evanston, IL 60208, USA
[8] Observatoire de Paris, LERMA, Collége de France, CNRS, PSL University, Sorbonne University, 75014 Paris, France
[9] Observatorio Astronómico Nacional (OAN-IGN) – Observatorio de Madrid, Alfonso XII, 3, 28014 Madrid, Spain
[10] National Astronomical Observatory of Japan, 2-21-1 Osawa, Mitaka, Tokyo 181-8588, Japan
[11] William H. Miller III Department of Physics and Astronomy, Johns Hopkins University, Baltimore, MD 21218, USA
[12] Department of Astronomy, University of Wisconsin-Madison, 475 N Charter Street, Madison, WI 53706, USA
[13] Department of Astronomy, University of Virginia, 530 McCormick Road, Charlottesville, VA 22903, USA
[14] National Radio Astronomy Observatory, 520 Edgemont Road, Charlottesville, VA 22903, USA
[15] Section of Astrophysics, Astronomy, and Mechanics, Department of Physics, National and Kapodistrian University of Athens, Panepistimioupolis Zografou, 15784 Athens, Greece
[16] Finnish Centre for Astronomy with ESO (FINCA), University of Turku, Väisäläntie 20, FI-21500 Piikkiö, Finland

ABSTRACT

Context. Molecular gas plays a critical role in regulating star formation and nuclear activity in galaxies. Sulphur-bearing molecules, such as H₂S, are sensitive to the physical and chemical environments in which they reside and are potential tracers of shocked, dense gas in galactic outflows and active galactic nuclei (AGNs).

Aims. We aim to investigate the origin of H₂S emission and its relation to dense gas and outflow activity in the central regions of nearby infrared-luminous galaxies.

Methods. We present Atacama Large Millimeter/submillimeter Array (ALMA) Band 5 observations of the ortho-H₂S $1_{1,0}-1_{0,1}$ transition in three nearby galaxies: NGC 1377, NGC 4418, and NGC 1266. We performed radiative transfer modelling using RADEX to constrain the physical conditions of the H₂S-emitting gas and compare the results to ancillary CO and continuum data.

Results. We detect compact H₂S emission in all three galaxies, arising from regions smaller than ∼150 pc. The H₂S spectral profiles exhibit broad line wings, suggesting an association with outflowing or shocked gas. In NGC 4418, H₂S also appears to be tracing gas that is counter-rotating. A peculiar redshifted emission feature may be inflowing gas, or possibly a slanted outflow. RADEX modelling indicates that the H₂S-emitting gas has high densities ($n_{H_2} \gtrsim 10^7$ cm^{-3}) and moderately warm temperatures (40−200 K). The derived densities exceed those inferred from CO observations, implying that H₂S traces denser regions of the ISM.

Key words. radiative transfer – galaxies: individual: NGC 4418 – galaxies: individual: NGC 1266 – galaxies: individual: NGC 1377 – galaxies: jets – galaxies: nuclei

1. Introduction

Molecular gas plays a crucial role in star formation and fuelling supermassive black holes (SMBHs), and bursts of star formation are particularly prevalent during collisions of gas-rich galaxies. Galaxy interactions can channel large quantities of material into the nuclei of luminous and ultra-luminous infrared galaxies (LIRGs/ULIRGs) (Sanders & Mirabel 1996; Iono et al. 2009). Furthermore, molecular gas provides key insights into physical processes such as massive outflows driven by nuclear activity (e.g. Sturm et al. 2011; Feruglio et al. 2011; Chung et al.

2011; Aalto 2012; Aalto et al. 2012a, 2015; Cicone et al. 2014; Sakamoto et al. 2014; Fluetsch et al. 2019; Veilleux et al. 2020). Such outflows regulate the growth of galactic nuclei, and the momentum they carry suggests that the central regions of these galaxies might be cleared of gas within just a few million years (e.g. Feruglio et al. 2011; Cicone et al. 2014). However, the morphology of such molecular feedback varies widely, from wide-angle winds (Veilleux et al. 2013) and gas entrained by radio jets (Morganti et al. 2015; García-Burillo et al. 2015; Dasyra et al. 2016), to tightly collimated molecular outflows (Aalto et al. 2016; Sakamoto et al. 2017; Barcos-Muñoz et al. 2018; Falstad et al. 2019).

[*] Corresponding author: mamiko@chalmers.se

The ultimate fate of the molecular gas, however, remains unclear. One outstanding question is whether this gas escapes the galaxy or returns to fuel new episodes of activity (e.g. Pereira-Santaella et al. 2018; Lutz et al. 2020). The nature of the molecular phase in outflows is also uncertain; we would like to know if they consist of molecular clouds swept out of the circumnuclear disc or if molecular clouds can form in situ within the outflow (e.g. Ferrara & Scannapieco 2016). Moreover, it is not known whether clouds in the outflow expand and evaporate or condense and potentially form stars while embedded in the outflow (Maiolino et al. 2017). To address these questions, we need detailed studies of the physical conditions of the molecular gas in outflows to understand its origins, evolution, and how these processes are linked to the driving mechanisms of the outflows.

Besides CO, a range of molecular species, including HCN, HCO$^+$, HNC, CN, and HC$_3$N, are essential tools for probing cloud properties in external galaxies. Due to their high dipole moments, these molecules typically require high gas densities ($n > 10^4$ cm^{-3}) to produce emission from even their low-J rotational transitions. Consequently, they are more directly associated with dense star-forming regions than, for example, the lower J transitions of CO, as shown by Gao & Solomon (2004).

The detection of luminous HCN and CN emission within molecular outflows, indicates the presence of significant amounts of dense molecular gas (e.g. Aalto 2012; Sakamoto et al. 2014; Matsushita et al. 2015; García-Burillo et al. 2015; Privon et al. 2015; Walter et al. 2017; Harada et al. 2018; Cicone et al. 2020; Saito et al. 2022). However, it should also be noted that faint but widespread HCN emission may arise from more diffuse molecular gas as well (e.g. Nishimura et al. 2017).

To discern the origin of this dense gas, we need tracers sensitive to specific physical and chemical environments. Being one of the most chemically reactive elements (e.g. Mifsud et al. 2021), sulphur exhibits strong sensitivity to the kinetic and thermal state of the gas. Sulphur-bearing molecules, such as H$_2$S, SO, and SO$_2$, tend to be unusually abundant in regions with high-mass star formation (0.1−1.0 pc size region), particularly where shocks or elevated temperatures are present (e.g. Mitchell 1984; Minh et al. 1990; Van der Tak et al. 2003; Fontani et al. 2023; Martinez et al. 2024). Observations of these sulphur-bearing species can therefore help constrain the properties of dense gas in outflows.

H$_2$S is thought to be the dominant sulphur-bearing molecule on icy grain mantles, as sulphur readily undergoes hydrogenation on dust surfaces, despite its lack of detection in interstellar ices (Charnley 1997; Wakelam et al. 2004; Viti et al. 2004; Bariosco et al. 2024). Consequently, in quiescent star-forming regions, H$_2$S is generally found in low gas-phase abundances due to its depletion onto grains. However, shocks can liberate H$_2$S from the grains, injecting it into the gas phase. This is supported by theoretical studies (e.g. Woods et al. 2015) showing clear evidence for enhanced H$_2$S abundances in warm and shocked gas. In particular, Holdship et al. (2017) showed that the propagation of a C-type[1] shock through a cloud can efficiently form H$_2$S, resulting in a significant abundance increase in the post-shock gas. The chemical evolution of H$_2$S, along with its connection to

grain processing, shares similarities with water (H$_2$O) chemistry. However, an observational advantage is that H$_2$S has a ground-state transition at $\lambda = 2$ mm, which is accessible to ground-based telescopes.

For the reasons mentioned above, H$_2$S emerges as a sensitive tracer for studying outflows and obscured nuclear activity in galaxies (Sato et al. 2022). Observations of the ground-state transition of H$_2$S ($1_{1,0}-1_{0,1}$ at 168.7 GHz) towards 12 nearby LIRGs detected emission in nine sources, with simultaneous HCN and HCO$^+$ line measurements. While H$_2$S abundance ratios relative to HCN and HCO$^+$ showed no clear connection to galactic-scale molecular outflows, its line luminosity correlated more strongly with outflow mass than traditional CO tracers. This suggests H$_2$S enhancement likely arises from small-scale shocks in nuclear regions rather than large-scale outflow activity. To resolve the emission sources, follow-up Atacama Large Millimeter/submillimeter Array (ALMA) observations achieved 0″.1−1″.2 spatial resolution towards three galaxies, enabling direct comparison between H$_2$S distribution and outflows.

This paper is organised as follows. Section 2 describes the galaxy sample and ALMA observations. Section 3 presents the observational results. In Section 4, we discuss the possible mechanisms for the formation of gas-phase H$_2$S and the origin of H$_2$S in the observed galaxies. Finally, Section 5 summarises our conclusions and provides future directions for understanding the role of H$_2$S as a tracer of dense gas and/or small-scale shocks.

2. Observations and data reduction

2.1. Sample selection

Sato et al. (2022) reported the detection of H$_2$S emission in nine infrared-luminous galaxies. These galaxies encompass a wide variety of evolutionary stages and environmental conditions. To further explore the evolution of galaxies with dusty dense cores, we selected a sub-group of three nearby galaxies, each exhibiting molecular outflows but at different stages of interaction: NGC 1377, NGC 4418, and NGC 1266. The target properties are given in Table 1. All of them are relatively infrared luminous ($L_{IR} = 10^{10}-10^{11} L_\odot$), suggesting that they host a dense dusty core. In the following, we provide a brief overview of the key characteristics of these three galaxies.

NGC 1377 ($z = 0.00598$) is a nearby lenticular galaxy at an estimated distance of 21 Mpc (1″ = 102 pc) and has an IR luminosity of $L_{IR} = 1.3 \times 10^{10} L_\odot$ (Sanders et al. 2003). A powerful molecular jet (with a mass outflow rate of 8−35 $M_\odot$ yr^{-1}) was found (e.g. Aalto et al. 2012b, 2016, 2020). It is also in the list of galaxies that host a compact obscured nucleus (CON; Falstad et al. 2021), which is identified with extremely high nuclear gas column density ($N_{H_2} > 10^{24}$ cm^{-2}). The nucleus is above the radio-FIR correlation (Spoon et al. 2006), though it is unclear whether the nucleus hosts a nascent starburst (Roussel et al. 2003, 2006) or a radio-quiet active galactic nucleus (AGN) due to the extreme dust obscuration in the centre (Imanishi 2006).

NGC 4418 is one of the nearest ($z = 0.00727$, 1″ = 150 pc) CON-hosting galaxies and is also a LIRG ($L_{IR} = 1.6 \times 10^{11} L_\odot$ Sanders et al. 2003). It is composed of an interacting system with the nearby galaxy VV 655. A kiloparsec-scale polar outflow has been reported (e.g. Sakamoto et al. 2013; Ohyama et al. 2019).

NGC 1266 ($z = 0.00724$, 1″ = 145 pc) is a non-interacting nearby S0 galaxy with a dense and compact molecular nucleus and a massive AGN-driven molecular outflow

---

[1] A C-type shock is a continuous, magnetically mediated shock in partially ionised gas where ions and neutrals decouple, unlike a J-type shock, which features a sharp, discontinuous jump in gas properties. The maximum velocity for a C-shock depends on the pre-shock gas density and magnetic-field strength, but is generally lower than for J-shocks (e.g. Draine & McKee 1993).

Table 1. Basic information of sources.

Object	RA (J2000)	Dec (J2000)	D_L [a] (Mpc)	L_{IR} [b] ($L_\odot$)	Type	Outflow [c]
NGC 1377	03:36:39.1	−20:54:08	21	1.3×10^{10}	AGN? with CON	(1)
NGC 4418	12:26:54.6	−00:52:39	31.9	1.6×10^{11}	AGN with CON	(2)
NGC 1266	03:16:00.75	−02:25:38.5	29.9	2.9×10^{10}	AGN	(3)

Notes. [a]Distances taken from Sanders et al. (2003). [b]Infrared luminosities taken from Sanders et al. (2003). [c]References: (1) e.g. Aalto et al. (2012b, 2016), (2) Ohyama et al. (2019), (3) Alatalo et al. (2011), Davis et al. (2012).

Table 2. Description of the ALMA observations and the continuum results.

Object	Project ID	ν_{obs} [a] [GHz]	b_{min}, b_{max} [m]	t_{int} [b] [h]	$\theta_{maj} \times \theta_{min}$ [arcsec^2]	$I_{cont,peak}$ [mJy beam^{-1}]	rms$_{cont}$ [c] [mJy beam^{-1}]	S_{cont} [d] [mJy]
NGC 1377	2018.1.00423.S	167.76	67/585	1.1	0″.51 × 0″.43	0.198	0.011	0.30 ± 0.013
	2018.1.01488.S	216.71	15/13900	1.1	0″.10 × 0″.08	0.178	0.018	0.28 ± 0.02
	2018.1.01488.S	691.47	37/1154	1.1	0″.19 × 0″.15	9.65	0.407	31.5 ± 2.4
NGC 4418	2018.1.00939.S	167.575	155/1500	0.4	0″.21 × 0″.16	18.4	0.076	23.4 ± 0.15
	2012.1.00377.S	216.71	15/1600	0.1	0″.37 × 0″.23	24.1	0.643	45.0 ± 1.18
NGC 1266	2018.1.00423.S	167.55	66/565	0.9	0″.52 × 0″.47	2.59	0.013	3.84 ± 0.11
	2011.1.00511.S	216.71	21/384	1.4	1″.26 × 0″.82	5.22	0.120	5.74 ± 0.24

Notes. [a]Central frequency of the spectral window which include the targeted line. [b]On-source observation time. [c]Noise level determined using CLASS package in GILDAS (http://www.iram.fr/IRAMFR/GILDAS). [d]Flux density determined with CASA from the region with over 3σ emission for each source.

from its central region (Alatalo et al. 2011; Alatalo 2015). Similar to NGC 4418, the nature of its nuclear activity remains ambiguous, with both AGN and compact starburst scenarios being viable explanations for its energetic emission and outflow properties (Nyland et al. 2013; Alatalo 2015). Furthermore, shocks are widespread throughout the galaxy's interstellar medium, evidenced by highly excited H_2 emission and disturbed ionised gas kinematics, which are likely driven by interactions between the AGN-driven outflow and dense circumnuclear gas (Pellegrini et al. 2013; Otter et al. 2024).

2.2. ALMA Observations

The observations in the ortho-H_2S $1_{1,0}-1_{0,1}$ line were carried out with ALMA in October 2018 for NGC 1377 and NGC 1266 (2018.1.00423.S) and in August 2019 for NGC 4418 (2018.1.00939.S), respectively, using the Band 5 receivers (Belitsky et al. 2018). The correlator was set up with two 1.875 GHz-wide (480 channels) spectral windows for NGC 1377 and NGC 1266, and four 1.875 GHz-wide (240 channels) spectral windows for NGC 4418, such that one of the windows was centred at the redshifted H_2S $1_{1,0}-1_{0,1}$ line (ν_{rest} = 168.763 GHz, E_u = 27.9 K).

Complementary data of the para-H_2S $2_{2,0}-2_{1,1}$ line (ν_{rest} = 216.710 GHz, E_u = 84.0 K) were obtained from the ALMA archive: project code 2018.1.01488.S for NGC 1377, 2012.1.00375.S for NGC 4418, and 2011.0.00511.S for NGC 1266 in Band 6 (Ediss et al. 2004). Finally, data of the CO 6−5 transition were included in the analysis. The ALMA observations of NGC 1377 in the CO (6−5) line were carried out from December 2018 to January 2021 for project code 2018.1.01488.S. The Band 9 receiver was used (Baryshev et al. 2015). The redshifted CO (6−5) line was covered in one of the four 1.875 GHz-wide (960 channels) spectral windows, centred at 687.491 GHz.

2.3. Data reduction

For each source, we used the calibrated data sets provided by the ALMA calibration pipeline. We fitted and subtracted the continuum in the *uv* plane through the CASA task 'uvcontsub'. We used a zeroth-order polynomial for the fit and estimated the continuum emission in the line-free frequencies. Images of the sources were produced using the 'tclean' task in CASA with natural weighting. A spectral binning of Δv = 20 km s^{-1} was applied. The typical angular resolution is 0″.2−0″.5. A summary of the observations is given in Table 2.

3. Results

The H_2S $1_{1,0}-1_{0,1}$ transition line is detected in emission towards all three galaxies. Figures 1, 5, and 7 show the integrated intensity maps and spectra of this line for the three galaxies, respectively. We also present the detection of the H_2S $2_{2,0}-2_{1,1}$ transition line in Figs. 2, 6, and 8, for which we obtained the data from the ALMA archive. Towards NGC 1377, archival data also show a detection of CO 6−5. The spectra, the continuum emission, and the integrated intensity map for this added data set are shown in Fig. 3 in the same manner as for H_2S.

Panel c in each Figs. 1−8 shows the spectrum taken from the region within the 3σ contour in the moment-zero image. Panel d in each Figs. 1−8 shows the spectrum taken from the central pixel. The H_2S $1_{1,0}-1_{0,1}$ and H_2S $2_{2,0}-2_{1,1}$ lines with higher signal-to-noise ratios show profiles that appear to include high-velocity wings. We found that a single Gaussian component is insufficient to adequately fit these lines, but another component is required. The individual Gaussian fits (dashed and dotted lines), along with the combined fits (solid grey line), are shown with the spectra of the galaxies (black histogram) in all spectra except the ones for H_2S $2_{2,0}-2_{1,1}$ in NGC 1377 and NGC 1266, the lines of which have a lower signal-to-noise ratio and could
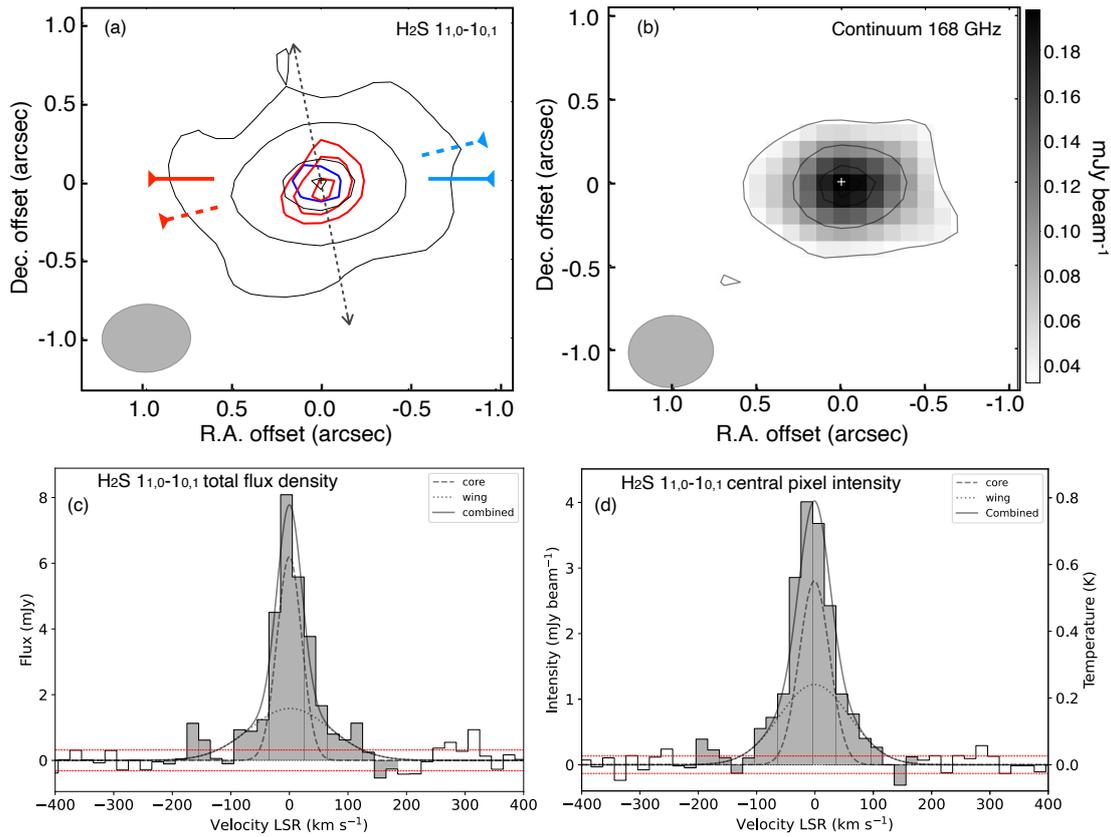
Fig. 1. Results of 168 GHz observations towards NGC 1377. (a) The velocity-integrated line emission maps of H_2S $1_{1,0}-1_{0,1}$. Black contours: $-70\,\mathrm{km\,s^{-1}}$ to $70\,\mathrm{km\,s^{-1}}$ (3, 9, 27, and 36σ, where $\sigma_{core} = 6.94 \times 10^{-3}\,\mathrm{Jy\,beam^{-1}\,km\,s^{-1}}$); blue: $-200\,\mathrm{km\,s^{-1}}$ to $-100\,\mathrm{km\,s^{-1}}$; red: $100\,\mathrm{km\,s^{-1}}$ to $200\,\mathrm{km\,s^{-1}}$, where $\sigma_{red} = 9.35 \times 10^{-3}\,\mathrm{Jy\,beam^{-1}\,km\,s^{-1}}$ and $\sigma_{blue} = 9.38 \times 10^{-3}\,\mathrm{Jy\,beam^{-1}\,km\,s^{-1}}$, respectively). The beam size is shown in the bottom left by a grey-filled circle. The blue and red line segments indicate the position angle (PA) of the disc. The PA of the nuclear continuum is $90°$ (scales of $r = 2\,\mathrm{pc}$), and the orientation of the dynamics of the nuclear disk is also close to $90°$ (Aalto et al. 2020). Aalto et al. (2020) noted that this is different from the $104°$ found for the major axis on larger scales of $r = 10\,\mathrm{pc}$ (Aalto et al. 2016). The direction of the molecular outflows detected in CO $3-2$ (PA $\sim 11°$, Fig. 4, Aalto et al. 2016) is indicated with a black dotted line. (b) The continuum emission at 168 GHz is shown in greyscale and contours (3, 9, 15, and 17σ, where $\sigma_{cont} = 1.1 \times 10^{-5}\,\mathrm{Jy\,beam^{-1}}$). (c) Spectrum in the unit of the flux density within the emitting region (over 3σ in moment-0 image) against the line velocity offset at the systemic velocity. The black histogram shows the observation result. The red dotted line indicates the 1σ rms level. The black dashed line shows the narrow line component, the dotted line indicates the broad line component, and the solid line shows two components combined. (d) Spectrum in units of the mean brightness at the peak intensity pixel against the line velocity.

be adequately fitted with only one Gaussian component. The red dotted line indicates the 1σ noise level.

In Table 3, the parameters of the Gaussian fits are listed together with the velocity-integrated flux densities. Velocity-integrated intensity maps were created by integrating the emission over different velocity ranges, and these are shown as contours of different colours in the images. The integration velocity ranges for each source are further discussed below.

3.1. Line emission for individual sources

Line emissions of NGC 1377, NGC 4418, and NGC 1266 exhibit a number of common features in their line profiles and spatial distributions. In all galaxies, the H_2S $1_{1,0}-1_{0,1}$ line shows prominent high-velocity wings that cannot be fitted with a single Gaussian, requiring at least two components: a narrow, bright core and a broader, fainter wing. The velocity-integrated emission maps reveal centrally peaked structures for all lines, with the core emission typically arising from compact regions of $100-300\,\mathrm{pc}$ in diameter, sometimes exhibiting slight elongation along specific directions. The wing components are even more concentrated, generally overlapping with the continuum peaks. Their spatial distribution shows slight directional extension, suggesting motions such as outflows. In summary, these trends indicate that all three galaxies harbour compact nuclear regions with signs of outflows or other energetic processes affecting their molecular gas.

3.1.1. NGC 1377

The line profiles of H_2S $1_{1,0}-1_{0,1}$ exhibit clear high-velocity wings that cannot be fitted with a single Gaussian component. A double Gaussian fit shows that one of the Gaussians is narrow and brighter, which we refer to as the core component, and the other is broader and less bright, which we refer to as the wings (see Table 3). From the Gaussian fits to H_2S $1_{1,0}-1_{0,1}$, it is found that the core component exhibits a line width of $\sim 60\,\mathrm{km\,s^{-1}}$, while the broader component has a width of $\sim 130\,\mathrm{km\,s^{-1}}$.

Forcing the central velocity to be the same as for the H_2S $1_{1,0}-1_{0,1}$ line, the H_2S $2_{2,0}-2_{1,1}$ line exhibits a line width of
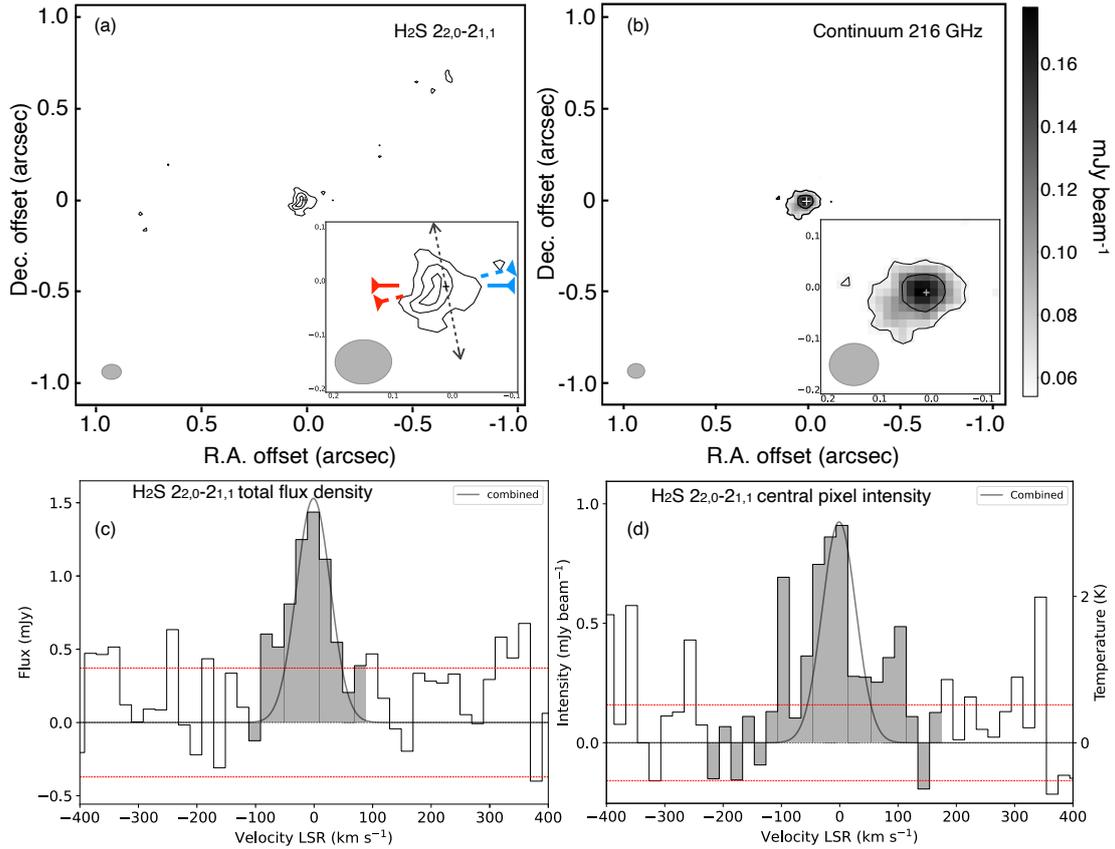
Fig. 2. Results of 216 GHz observations towards NGC 1377. (a) The velocity-integrated line emission maps of H_2S $2_{2,0}-2_{1,1}$: $-100\,\mathrm{km\,s^{-1}}$ to $100\,\mathrm{km\,s^{-1}}$ (2, 3, 4, and 5σ, where $\sigma = 2.1 \times 10^{-2}\,\mathrm{Jy\,beam^{-1}\,km\,s^{-1}}$). The lines and symbol conventions are the same as in Fig. 1. (b) The continuum emission at 216 GHz is shown in greyscale and contours (3, 6, and 9σ, where $\sigma_{\mathrm{cont}} = 1.8 \times 10^{-5}\,\mathrm{Jy\,beam^{-1}}$). (c) Spectrum in the unit of the flux density within the emitting region (over 3σ in moment-0 image) against the line-velocity offset at the systemic velocity. The black histogram shows the observation result. The red dotted line indicates the 1σ rms level. The black solid line represents the single Gaussian fit. (d) Spectrum in units of the mean brightness at the peak intensity pixel against the line velocity.

$\sim70\,\mathrm{km\,s^{-1}}$. This is the width for the whole line because the signal-to-noise ratio is too low to meaningfully separate it into narrow and broad components. The CO 6−5 line also needs a double Gaussian fit for its line profile, exhibiting a line width of $\sim95\,\mathrm{km\,s^{-1}}$ for the line core component and $\sim175\,\mathrm{km\,s^{-1}}$ for the wing component.

We find a centrally peaked structure in the velocity integrated maps for all three lines (Figs. 1–3). In H_2S $1_{1,0}-1_{0,1}$, the line core emission (corresponding to the narrow Gaussian component) comes from a region of 1″4 (around 150 pc) diameter from the centre, with a slight elongation in the west-east direction. The location of the line wing components are overlapping on top of the continuum peak of the galaxy, which is more compact in size than the emission corresponding to the line core component. The blueshifted emission is extended towards the north-east of the galaxy centre, while the redshifted emission is confined at the central beam-size region. The H_2S $2_{2,0}-2_{1,1}$ emission comes from a very compact region (0″17 ∼17 pc). In CO 6−5, the line-core emission comes from a slightly more extended region (1″6 diameter) than H_2S $1_{1,0}-1_{0,1}$, but it has similar tendency to extend more in the east-west direction compared to the north-south one. The blue- and redshifted emissions are extended in the opposite direction to each other: north-east and south-west, respectively. Both are within the range of the core component. Figure 4 shows a comparison between CO 6−5 and CO 3−2 high-velocity gas in NGC 1377. It shows an excita-

tion gradient along the axis of the outflow with CO 6−5 tracing warmer and/or dense gas at the beginning of the outflow (30−50 pc). It also shows a slight deviation from the indicated jet axis with a more north-south orientation. This is consistent with the notion of a precessing or swirling jet as discussed in Aalto et al. (2016, 2020).

3.1.2. NGC 4418

Similarly to NGC 1377, the line profiles of H_2S $1_{1,0}-1_{0,1}$ in NGC 4418 also exhibit clear high-velocity wings that cannot be fitted with a single Gaussian component. From the two Gaussian fits to H_2S $1_{1,0}-1_{0,1}$, it is found that the core component has a line width of $\sim107\,\mathrm{km\,s^{-1}}$, while the broader component has a width of $\sim353\,\mathrm{km\,s^{-1}}$ (Fig. 5d).

The line profile of the H_2S $2_{2,0}-2_{1,1}$ line in NGC 4418 is asymmetric, and we suspect that the excess in the blueshifted emission is a blending from an emission line of another species. Indeed, NGC 4418 has a very rich spectrum (e.g. Costagliola et al. 2015). One of the potential candidates for this blended feature is the ^{13}CN 2−1 line. Assuming that, we tried to fit three Gaussian components: two with the central velocity fixed to what we derived for the H_2S $1_{1,0}-1_{0,1}$ transition line (core and wings components), and one with the central velocity around $200\,\mathrm{km\,s^{-1}}$ offset from the central velocity of the H_2S line towards lower velocities. Thus, we found that the core
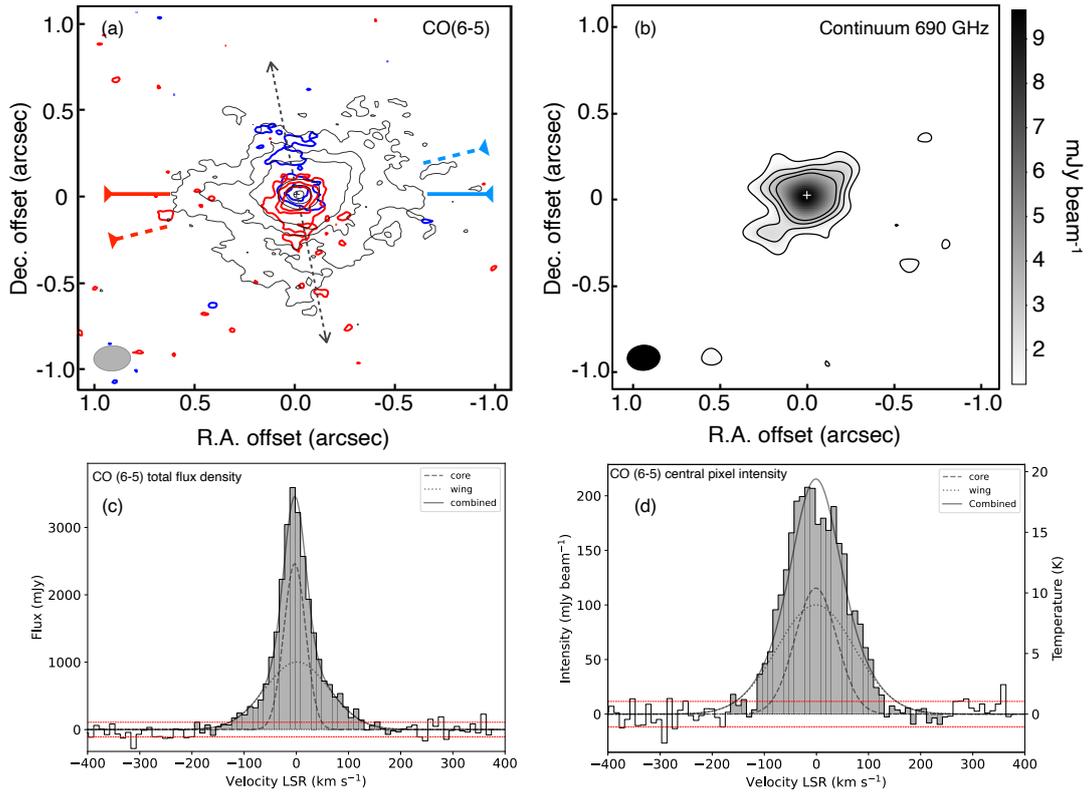
Fig. 3. Results of 691 GHz observations towards NGC 1377. (a) The velocity-integrated line emission maps of CO 6−5. Black contours: −70 km s^{-1} to 70 km s^{-1} (3, 6, 9, 27, and 36σ, where σ_{core} = 0.29 Jy beam^{-1} km s^{-1}); blue: −200 km s^{-1} to −100 km s^{-1}; red: 100 km s^{-1} to 200 km s^{-1} (3, 6, 9, and 12σ, where σ_{red} = 0.13 Jy beam^{-1} km s^{-1} and σ_{blue} = 0.16 Jy beam^{-1} km s^{-1}, respectively). The lines and symbol conventions are the same as in Fig. 1. (b) The continuum emission at 691 GHz in greyscale and contours: (3, 5, 7, and 9σ, where σ_{cont} = 4.07 × 10^{-1} Jy beam^{-1}). (c) Spectrum in the unit of the flux density within the emitting region (over 3σ in moment-0 image) against the line-velocity offset at the systemic velocity. The black histogram shows the observation result. The red dotted line indicates the 1σ rms level. The black dashed line shows the narrow line component, the dotted line shows the broad line component, and the solid line represents the two components combined. (d) Spectrum in units of the mean brightness at the peak intensity pixel against the line velocity.
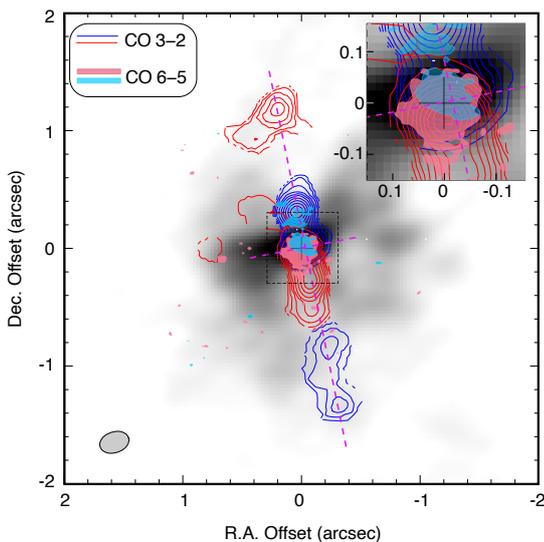
component has a similar line width to that for H$_2$S $1_{1,0}-1_{0,1}$ line, ~109 km s^{-1}, and the broader component has a width of ~236 km s^{-1}.

We find a centrally peaked structure in the velocity integrated maps for both lines (Figs. 5 and 6). In H$_2$S $1_{1,0}-1_{0,1}$, the line core emission comes from a region of 1″0 (around 150 pc) diameter from the centre. There is a slight elongation in the north-east direction that is not detected in the continuum emission. The location of the line wing components are overlapping on top of the continuum peak of the galaxy, which is more compact in size than the emission corresponding to the line core component. The blueshifted emission is extended towards the south-east of the galaxy centre and the redshifted emission is clearly directed towards the south-west of the centre.

The H$_2$S $2_{2,0}-2_{1,1}$ emission also comes from a similar region to H$_2$S $1_{1,0}-1_{0,1}$ (1″). The north-east elongation is more apparent. The line wings components are coming from the central beam region. The whole line emission shows almost the same distribution as the continuum emission.

3.1.3. NGC 1266

The H$_2$S $1_{1,0}-1_{0,1}$ line in NGC 1266 exhibits a clear redshifted emission. Such a line-wing emission was not detected on the blueshifted side of the line. There seems to be no candidate species that has a transition on the redshifted side of the H$_2$S

Fig. 4. Velocity-integrated map of CO 3−2 (Aalto et al. 2016). Greyscale shows the emission close to systemic velocity. The high-velocity emission from the molecular jet is shown in contours (with the red and blue showing velocity reversals along the axis). The vertical bar indicates a scale of 100 pc. For details of the figure, see Aalto et al. (2016). We indicate the extent and orientation of the CO 6−5 high velocity gas (from Fig. 3) with light blue and yellow ovals.
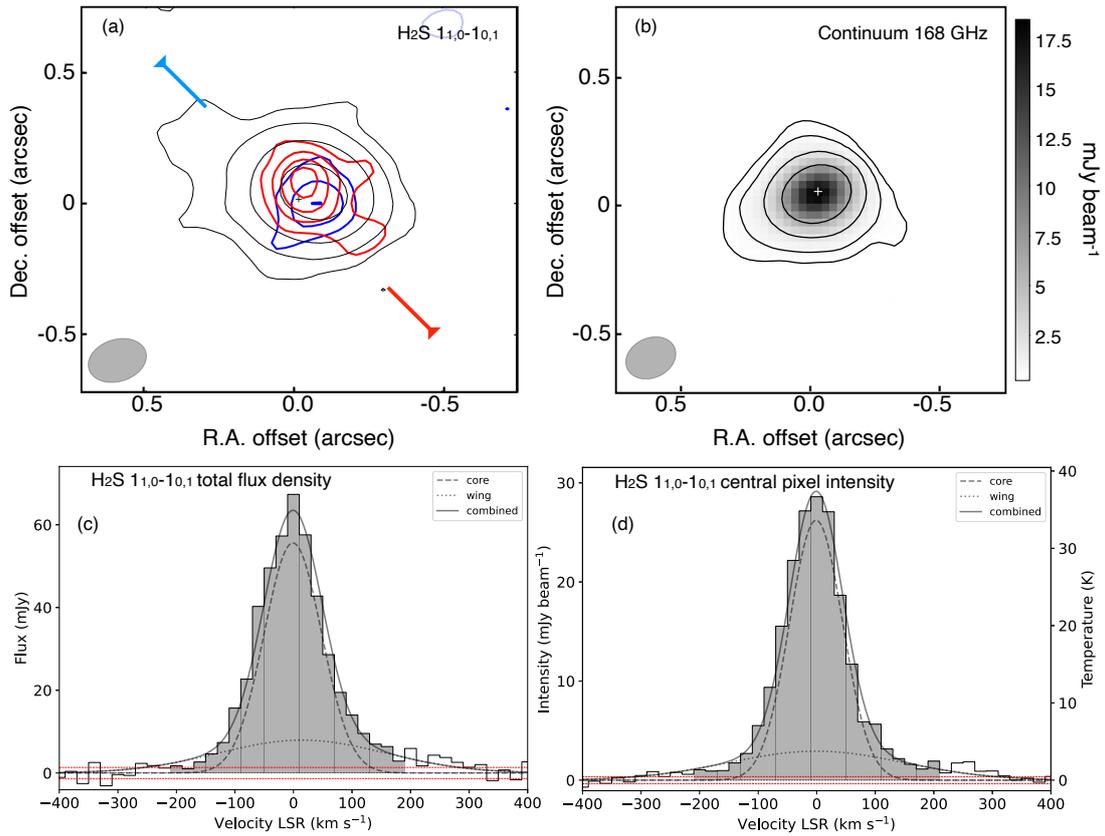
Fig. 5. Results of 168 GHz observations towards NGC 4418. (a) The velocity-integrated line-emission maps of H_2S $1_{1,0}-1_{0,1}$. Black contours: $-100 \, \mathrm{km \, s^{-1}}$ to $100 \, \mathrm{km \, s^{-1}}$ (3, 9, 27, 81, and 243σ, where $\sigma_{\mathrm{core}} = 2.63 \times 10^{-2} \, \mathrm{Jy \, beam^{-1} \, km \, s^{-1}}$); blue: $-200 \, \mathrm{km \, s^{-1}}$ to $-100 \, \mathrm{km \, s^{-1}}$; red: $100 \, \mathrm{km \, s^{-1}}$ to $200 \, \mathrm{km \, s^{-1}}$ (3, 4, 6, and 9σ, where $\sigma_{\mathrm{red}} = 2.41 \times 10^{-2} \, \mathrm{Jy \, beam^{-1} \, km \, s^{-1}}$ and $\sigma_{\mathrm{blue}} = 2.28 \times 10^{-2} \, \mathrm{Jy \, beam^{-1} \, km \, s^{-1}}$, respectively). The beam size is shown in the bottom left as a grey-filled circle. The blue and red line segments indicate the position angle (PA) of the disc ($\sim45°$, Costagliola et al. 2013). (b) The continuum emission at 168 GHz is shown in greyscale and as contours: (3, 9, 27, and 81σ, where $\sigma_{\mathrm{cont}} = 7.6 \times 10^{-5} \, \mathrm{Jy \, beam^{-1}}$). (c) Spectrum in the unit of the flux density within the emitting region (over 3σ in moment-0 image) against the line velocity offset at the systemic velocity. The black histogram shows the observation result. The red dotted line indicates the 1σ rms level. The black dashed line shows a narrow line component, the dotted line shows a broad line component, and the solid line represents the two components combined. (d) Spectrum in units of the mean brightness at the peak intensity pixel against the line velocity.

$1_{1,0}-1_{0,1}$ line ($100-200 \, \mathrm{km \, s^{-1}}$). So, we assume that the redshifted emission is part of the H_2S $1_{1,0}-1_{0,1}$ line. From the line profile (Figs. 7c and d), it seems that the line-wing components on the blueshifted side are absorbed. Looking at the moment-zero map (Fig. 7a), the blueshifted emission is not detected over 3σ. This type of line profile is consistent with an expanding gas observed against a warmer background-continuum source. The continuum emission arises from a compact, point-like source (Fig. 7b). If the absence of blueshifted emission is due to absorption, this absorption should be stronger at the central pixel than in the spectrum integrated over the extended emission region. The intensity profile extracted from the central pixel shows a minimum of approximately $0.7 \, \mathrm{mJy \, beam^{-1}}$, whereas the depth is only about $0.1 \, \mathrm{mJy \, beam^{-1}}$ when averaged over the 3σ emitting region (estimated by dividing the total flux in Fig. 7c by the solid angle of the emission region). This difference is consistent with absorption occurring against a compact continuum source. Thus, we applied three Gaussian fittings, two with the same central velocity and one with the central velocity as a free parameter, assuming that the blueshifted component of the line is absorbed due to the warm dust continuum at the centre. A line width of $\sim71 \, \mathrm{km \, s^{-1}}$ for the core component with a width of $\sim188 \, \mathrm{km \, s^{-1}}$ for the wing component could potentially fit the line profile.

The H_2S $2_{2,0}-2_{1,1}$ line in NGC 1266 was detected at the edge of the observed frequency band, and we cannot see the full width of the line, unfortunately. Thus, we fitted one Gaussian and obtained an estimation for a line width of $\sim50 \, \mathrm{km \, s^{-1}}$.

We find a centrally peaked structure in the velocity integrated maps for both lines (Figs. 7a and 8a). In H_2S $1_{1,0}-1_{0,1}$, the line-core emission comes from a region of $2''0$ (around 300 pc) diameter from the centre. The line-core component is distributed in a slightly larger region than the continuum emission. The redshifted component is detected from the nucleus to the north-east of the nucleus only in H_2S $1_{1,0}-1_{0,1}$. This direction agrees with the CO observations by Alatalo et al. (2011).

The H_2S $2_{2,0}-2_{1,1}$ emission is coming from a smaller region ($\sim1''$) than that of H_2S $1_{1,0}-1_{0,1}$. The emitting region is basically the observed beam size ($1''26 \times 0''82$); thus, it is not resolved.

3.2. Radiative-transfer modelling

We used the RADEX non-LTE radiative transfer code (Van Der Tak et al. 2007) to estimate the physical conditions (n_{H_2}, T_{kin}, N_{H_2S}) of the gas. We used the collision rates of H_2S, which are scaled from the full quantum calculations for collisional excitation of ortho- and para-H_2O by ortho- and para-H_2 from the references (Dubernet et al. 2006, 2009; Daniel et al.
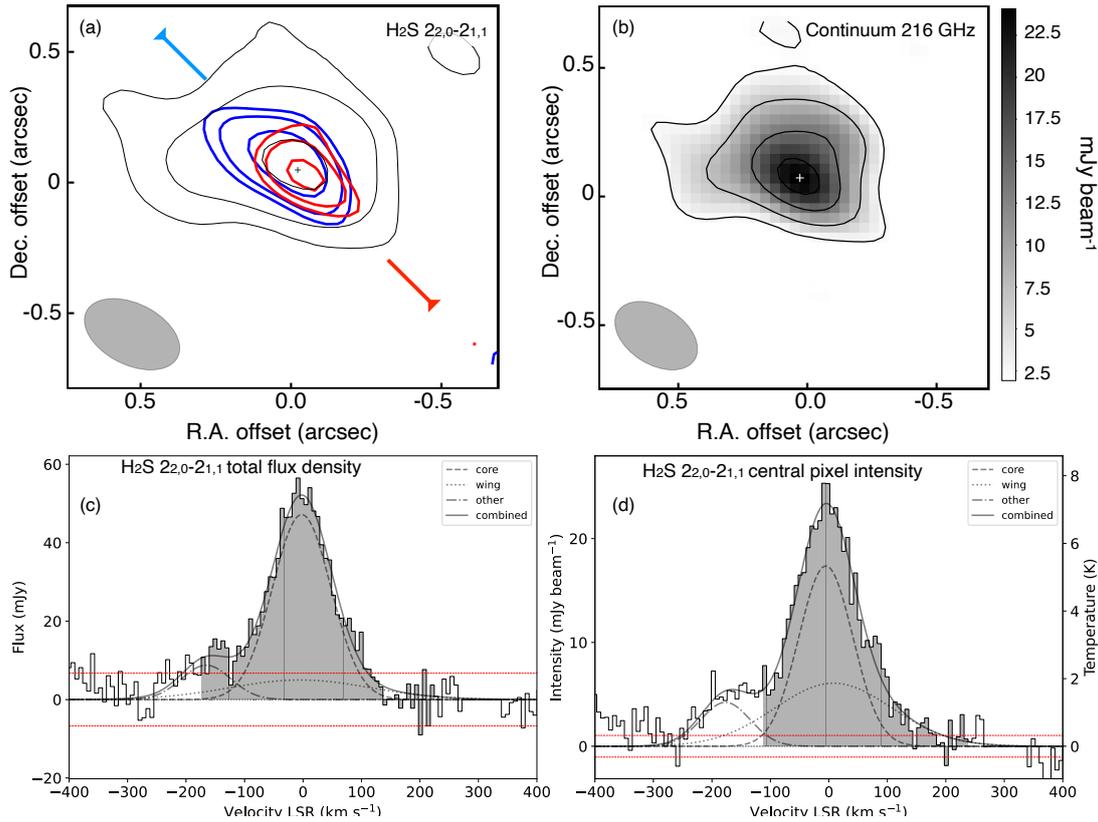
Fig. 6. Results of 216 GHz observations towards NGC 4418. (a) The velocity-integrated line-emission maps of $2_{2,0}-2_{1,1}$. Black contours: $-100\,\mathrm{km\,s^{-1}}$ to $100\,\mathrm{km\,s^{-1}}$ (3, 9, and 27σ, where $\sigma_{core} = 6.7 \times 10^{-2}\,\mathrm{Jy\,beam^{-1}\,km\,s^{-1}}$); blue: $-120\,\mathrm{km\,s^{-1}}$ to $-100\,\mathrm{km\,s^{-1}}$; red: $100\,\mathrm{km\,s^{-1}}$ to $200\,\mathrm{km\,s^{-1}}$ (3, 4, and 6σ, where $\sigma_{red} = 4.2 \times 10^{-2}\,\mathrm{Jy\,beam^{-1}\,km\,s^{-1}}$ and $\sigma_{blue} = 1.9 \times 10^{-2}\,\mathrm{Jy\,beam^{-1}\,km\,s^{-1}}$, respectively). The lines and symbol conventions are the same as in Fig. 5. (b) The continuum emission at 216 GHz shown in greyscale and by contours (3, 9, 27, and 81σ, where $\sigma_{cont} = 6.4 \times 10^{-4}\,\mathrm{Jy\,beam^{-1}}$). (c) Spectrum in the unit of the flux density within the emitting region (over 3σ in moment-0 image) against the line-velocity offset at the systemic velocity. The black histogram shows the observation result. The red dotted line indicates the 1σ rms level. The black dashed line shows a narrow line component, the dotted line shows a broad line component, the dash-dotted line represents other species (possibly 13CN line), and the solid line shows the three components combined. (d) Spectrum in units of the mean brightness at the peak intensity pixel against the line velocity.

2010, 2011). Additionally, we adopted an ortho-to-para ratio of 3 for H_2S ($H_2S\ 1_{1,0}-1_{0,1}$ is ortho, while $H_2S\ 2_{2,0}-2_{1,1}$ is para), corresponding to the thermal equilibrium value, and we assume that H_2S is primarily excited through collisions (Crockett et al. 2014). Given that each H_2S transition was observed with a different beam size, we adopted the smaller synthesised beam as the effective source size to minimise the impact of a beam mismatch on intensity measurements. While this simplification assumes considerable spatial overlap of the emitting regions for comparison purposes, we note that distinct spatial and velocity variations, discussed in Section 3.1, are acknowledged.

We explored molecular hydrogen densities, n_{H_2}, in the $10^4-10^8\,\mathrm{cm^{-3}}$ range (sampled in 40 logarithmically spaced steps), which brackets the critical densities $5.4 \times 10^5\,\mathrm{cm^{-3}}$ and $1 \times 10^6\,\mathrm{cm^{-3}}$ of the ortho- and para-H_2S transitions, respectively, at $T = 100\,\mathrm{K}$[2]. The H_2S column density, N_{H_2S}, is varied between 10^{14} and $10^{18}\,\mathrm{cm^{-2}}$ (sampled in 40 logarithmically spaced steps), consistently with the possibility of very high H_2 columns ($10^{24}\,\mathrm{cm^{-2}}$) and a typical H_2S abun-

dance of $10^{-10}-10^{-6}$ (Holdship et al. 2017; Crockett et al. 2014; Sato et al. 2022). Finally, we considered kinetic temperatures of $T_{kin} = 40-200\,\mathrm{K}$ with 15 steps evenly spaced on a linear scale and constrained by the observed H_2S brightness temperatures and previous CO-based temperature estimates (Aalto et al. 2016).

We compared the RADEX predictions to two observationally derived ratios for each source:

1. The peak-brightness temperature ratio, $T_{b,22}/T_{b,11}$, measured at the central pixel of the data cube.
2. The integrated-brightness temperature ratio, $\int T_{b,22}\mathrm{d}v / \int T_{b,11}\mathrm{d}v$, derived from the total velocity-integrated intensities.

The first ratio constrains the excitation under near-peak conditions, while the second ratio is more sensitive to the total column of emitting gas over the full line profile. We searched for model solutions that reproduce the observed ratio between these two quantities.

We used the average full width half maximum (FWHM) of each transition's core component as the velocity width input to RADEX, thereby excluding broad wings that may arise from outflows (separate features in the fitting). We list all final modelling parameters, along with their assumed ranges, in Table 4. Uncertainties may arise if any significant fraction of the line

---

[2] The critical densities, n_{crit} [$\mathrm{cm^3}$], are calculated as $n_{crit} = \frac{A}{a_{col}}$, where A [$\mathrm{s^{-1}}$] is the Einstein A-coefficient and a_{col} [$\mathrm{cm^{-3}\,s^{-1}}$] is the collisional rate coefficient. Values are from the molecular data from Leiden Atomic and Molecular Database (LAMDA: https://home.strw.leidenuniv.nl/~moldata/).
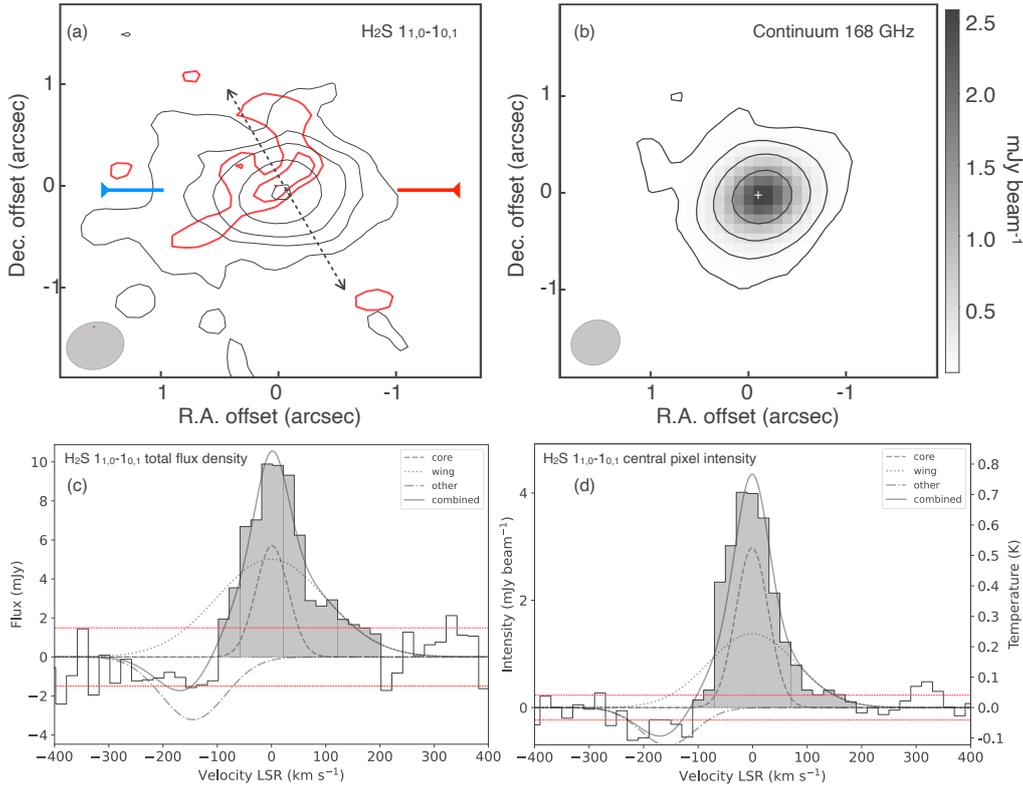
Fig. 7. Results of 168 GHz observations towards NGC 1266. (a) The velocity-integrated line-emission maps of H_2S $1_{1,0}-1_{0,1}$. Black contours: -70 km s^{-1} to 70 km s^{-1} (3, 6, 9, and 18σ, where $\sigma_{core} = 1.08 \times 10^{-2}$ Jy beam^{-1} km s^{-1}); blue: -100 km s^{-1} to -70 km s^{-1}; red: 70 km s^{-1} to 200 km s^{-1} (3, 4, and 5σ, where $\sigma_{red} = 7.5 \times 10^{-3}$ Jy beam^{-1} km s^{-1} and $\sigma_{blue} = 5.7 \times 10^{-3}$ Jy beam^{-1} km s^{-1}, respectively). The beam size is shown in the bottom left by a grey-filled circle. The blue and red line segments indicate the PA of the disc ($\sim 90°$) and direction of the molecular outflows detected in CO $2-1$ (PA $\sim 30°$) (Alatalo et al. 2011). (b) The continuum emission at 168 GHz is shown in greyscale and as contours (3, 9, 27, and 81σ, where $\sigma_{cont} = 1.3 \times 10^{-5}$ Jy beam^{-1}). (c) Spectrum in the unit of the flux density within the emitting region (over 3σ in moment-0 image) against the line-velocity offset at the systemic velocity. The black histogram shows the observation result. The red-dotted line indicates the 1σ rms level. The black dashed line shows a narrow line component, the dotted line shows a broad line component, the dash-dotted line shows an absorption component, and the solid line represents the three components combined. (d) Spectrum in units of the mean brightness at the peak intensity pixel against the line velocity.

emission (especially in the wings) originates from gas with different physical conditions.

Although this approach provides robust first-order constraints, we note several caveats: (a) partial beam dilution could reduce our line ratios if the true source size is smaller than the assumed beam; (b) scaling collision rates from H_2O introduces additional uncertainties for H_2S; (c) the assumed ortho-to-para (o/p) ratio of 3 may not apply to regions with non-thermal processes (e.g. in the Orion KL region, Crockett et al. 2014 calculated an o/p ratio of less than 2); (d) the RADEX modelling is constrained by only two H_2S transitions; and (e) the H_2S-emitting region could not be accurately described by a single phase as initially assumed. Despite these limitations, the models give a consistent picture of dense ($>10^6$ cm^{-3}) and warm ($T_{kin} > 40$ K) gas traced by H_2S.

3.2.1. Results for individual objects: NGC 1377

Using a line width of $\Delta v = 65$ km s^{-1}, we find that an H_2 density $n_{H_2} > 3 \times 10^6$ cm^{-3}, at any H_2S column density, N_{H_2S}, and kinetic temperature, T_{kin}, can adequately reproduce our observational results. Since this value is well above the critical density for both transitions, the gas traced by H_2S is most likely thermalised. The derived density is at least ten times higher than that

obtained from CO by Aalto et al. (2020), which reported a column density of $N_{H_2} = 1.8 \times 10^{24}$ cm^{-2} in the inner 2 pc region (beam size $= 0''.02$), corresponding to $n_{H_2} = 1 \times 10^5$ cm^{-3}.

3.2.2. Results for individual objects: NGC 4418

With a line width of $\Delta v = 108$ km s^{-1}, we find that an H_2 density $n_{H_2} > 1 \times 10^7$ cm^{-3}, at any H_2S column density N_{H_2S} and kinetic temperature T_{kin}, can reproduce our observational results (Fig. 9). Thus, we expect that H_2S traces the gas with an even higher n_{H_2} than those in NGC 1377. This inferred density exceeds previous estimates from CO observations. Prior studies suggest a stratified temperature and density structure, with a $300-500$ K layer in the nuclear region ($5-8$ pc) and a surrounding 160 K layer extending to ~ 40 pc (Costagliola et al. 2013, 2015; Sakamoto et al. 2021). Our modelling can not distinguish those two layers due to the limitation of the spatial resolutions.

3.2.3. Results for individual objects: NGC 1266

For a line width of $\Delta v = 56$ km s^{-1}, we find that an H_2 density of $n_{H_2} > 5 \times 10^7$ cm^{-3}, a kinetic temperature of $T_{kin} > 140$ K, and an H_2S column density of $N_{H_2S} = 1 \times 10^{14}$ cm^{-2} can reproduce our observational results. Notably, the modelling
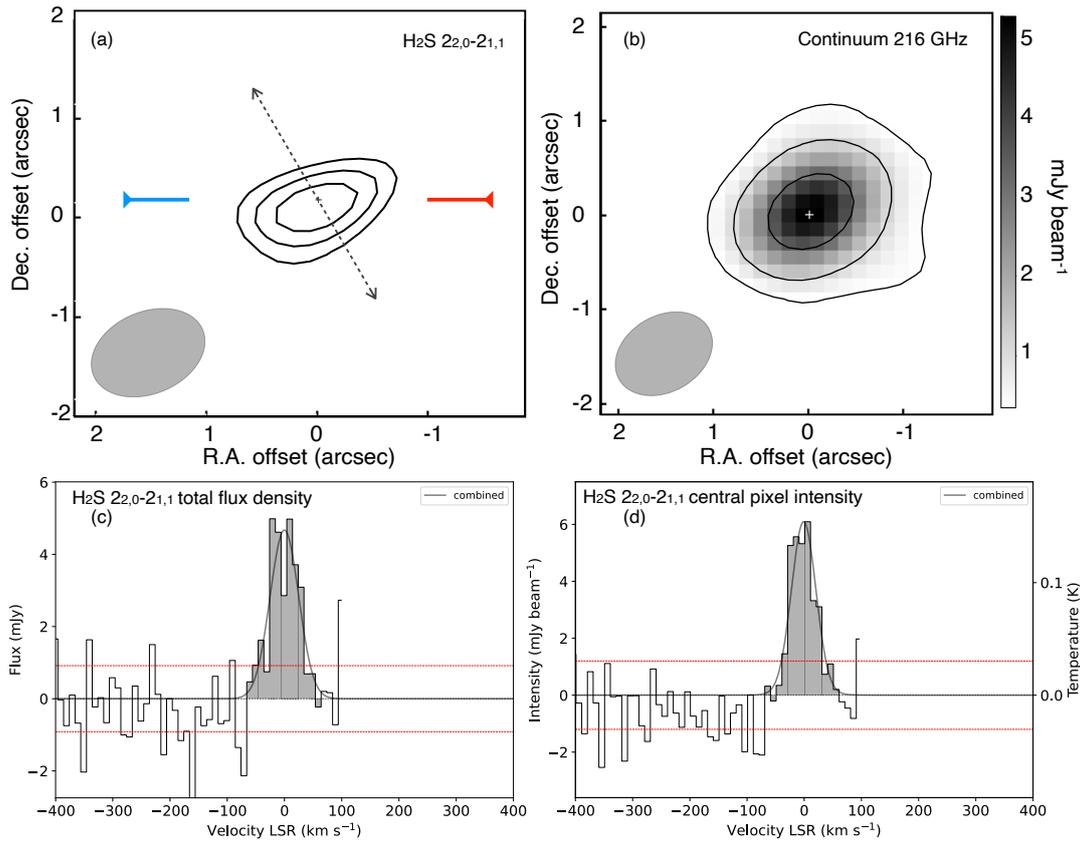
Fig. 8. Results of 216 GHz observations towards NGC 1266. (a) The velocity-integrated lineemission maps of $2_{2,0}-2_{1,1}$. Black contours: $-70\,\mathrm{km\,s^{-1}}$ to $70\,\mathrm{km\,s^{-1}}$ (3, 6, and 9σ, where $\sigma_{\mathrm{core}} = 1.08 \times 10^{-2}\,\mathrm{Jy\,beam^{-1}\,km\,s^{-1}}$). The lines and symbol conventions are the same as in Fig. 7. (b) The continuum emission at 216 GHz is shown in greyscale and via contours (3, 9, and 27σ, where $\sigma_{\mathrm{cont}} = 1.2 \times 10^{-4}\,\mathrm{Jy\,beam^{-1}}$). (c) Spectrum in the unit of the flux density within the emitting region (over 3σ in moment-0 image) against the line-velocity offset at the systemic velocity. The black histogram shows the observation result. The red dotted line indicates the 1σ rms level. The black solid line signals the Gaussian fit. (d) Spectrum in units of the mean brightness at the peak intensity pixel against the line velocity.

solutions were only found at this specific H_2S column density. Our results indicate an extremely high n_{H_2}, which is consistent with a highly dense environment. However, it should be noted that these values are averaged over the beam size, covering a region of $\sim75\,\mathrm{pc}$, potentially blending gas components with different densities and temperatures. For comparison, Alatalo et al. (2011) estimated a lower limit of $n_{H_2} \geq 6.9 \times 10^3\,\mathrm{cm^{-3}}$ from CO 1−0 observations of the central region with a radius of $\sim1''$ ($\sim150\,\mathrm{pc}$). The significant difference in derived densities likely reflects the use of different tracers and the higher critical density of H_2S, which allows us to probe denser regions within the beam.

3.3. Continuum emission

The continuum emission maps are presented in panel b of Figs. 1–8. Continuum emission was detected for all three sources. For the measurements of the total flux and the spatial extent of the emission, we only included signal above 3σ flux levels.

The size of the 168 GHz continuum emission in NGC 1377 is approximately $1.3'' \times 1.0''$ ($133 \times 102\,\mathrm{pc}$). The peak flux of this emission is $0.20\,\mathrm{mJy\,beam^{-1}}$ ($T_b = 1.5\,\mathrm{K}$), and the total flux, integrated over the region defined by the 3σ contour level, is $0.30 \pm 0.01\,\mathrm{mJy}$. The 216 GHz continuum emission in NGC 1377 arises from a more compact region with an

angular size of approximately $0.2''$ in diameter, corresponding to only 20 pc across the emitting region. The peak flux of this emission is $0.18\,\mathrm{mJy\,beam^{-1}}$ ($T_b = 3.5\,\mathrm{K}$), and the total flux, integrated over the region defined by the 3σ contour level, is $0.28 \pm 0.02\,\mathrm{mJy}$. The 691 GHz continuum-emitting region has a diameter of $0.8''$ (82 pc), with significantly higher total and peak fluxes of $32 \pm 2\,\mathrm{mJy}$ and $9.7\,\mathrm{mJy\,beam^{-1}}$ ($T_b = 14\,\mathrm{K}$), respectively, compared to those at 168 GHz and 216 GHz. As shown in Figs. 1, 2, and 3, while the 691 GHz continuum emission is spatially resolved by the synthesised beam, the emission at 168 GHz and 216 GHz is not resolved.

NGC 4418 exhibits similar sized continuum regions but higher fluxes at both measured frequencies compared to the continuum emission of NGC 1377. The 168 GHz continuum-emitting region in NGC 4418 has a diameter of approximately $0.5''$ (80 pc). The peak flux of this emission is $18\,\mathrm{mJy\,beam^{-1}}$ ($T_b = 28\,\mathrm{K}$), and the total flux, integrated over the region defined by the 3σ contour level, is $23.4 \pm 0.2\,\mathrm{mJy}$. The size of the 216 GHz continuum emission in NGC 4418 has an angular size of $1.0''$ (165 pc). The peak flux of this emission is $24.1\,\mathrm{mJy\,beam^{-1}}$ ($T_b = 12\,\mathrm{K}$), and the total flux is $45.0 \pm 1.2\,\mathrm{mJy}$.

NGC 1266 has the largest continuum-emitting region among the three galaxies, with a diameter of 290 pc at both frequencies. The peak flux of the 168 GHz continuum emission is $2.6\,\mathrm{mJy\,beam^{-1}}$ ($T_b = 2.8\,\mathrm{K}$) and the total flux is $3.8 \pm 0.1\,\mathrm{mJy}$. The 216 GHz continuum emission within the 3σ contour region

Table 3. Observations results.

	Central beam				3σ region			
	FWHM [km s^{-1}]	v_{centre} [km s^{-1}]	I_{peak} [mJy beam^{-1}]	$\int S\,dv$ [1] [Jy beam^{-1} km s^{-1}]	FWHM [km s^{-1}]	v_{centre} [km s^{-1}]	I_{peak} [mJy]	$\int S\,dv$ [1] [Jy km s^{-1}]
NGC 1377								
H$_2$S 1−1 Total	80 ± 3	3 ± 1	3.9 ± 0.1	0.36 ± 0.01	67 ± 4	1 ± 2	7.3 ± 0.4	0.52 ± 0.04
Core	57 ± 10	1 ± 2	2.7 ± 0.7	0.17 ± 0.05	50 ± 6	0 ± 2	6.2 ± 0.8	0.33 ± 0.06
Wings	129 ± 28	7 ± 7	1.4 ± 0.8	0.20 ± 0.10	163 ± 45	1 ± 12	1.6 ± 0.7	0.27 ± 0.15
H$_2$S 2−2 Core	68 ± 36	−1 ± 5	0.9 ± 0.4	0.07 ± 0.05	68 ± 27	−1 ± 12	1.5 ± 0.5	0.1 ± 0.06
CO(6−5) Total	138 ± 3	−2 ± 1	207 ± 4	30 ± 1	77 ± 2	−3 ± 1	2.9 ± 0.1 Jy	239 ± 9
Core	94 ± 25	0 ± 3	115 ± 71	11.7 ± 7.8	50 ± 3	−3 ± 1	2.5 ± 0.1	129 ± 10
Wings	175 ± 39	0 ± 6	100 ± 73	18.6 ± 14.2	144 ± 11	1 ± 3	1.0 ± 0.1	154 ± 26
NGC 4418								
H$_2$S 1−1 Total	121 ± 4	−5 ± 2	29 ± 1	4.1 ± 0.1	134 ± 5	−4 ± 2	62 ± 2	9.6 ± 0.3
Core	107 ± 4	−1 ± 1	27 ± 1	3.0 ± 0.1	115 ± 5	−7 ± 1	56 ± 2	6.8 ± 0.4
Wings	353 ± 60	−1 ± 16	2.9 ± 0.8	1.1 ± 0.4	312 ± 40	18 ± 26	8.6 ± 2.2	2.8 ± 0.8
H$_2$S 2−2 Total	155 ± 11	−6 ± 5	22 ± 1	4.1 ± 0.1	141 ± 11	−5 ± 5	50 ± 3	8.2 ± 0.2
Core	109 ± 18	−5 ± 6	17 ± 5	2.0 ± 0.7	118 ± 22	−2 ± 6	47 ± 7	5.9 ± 2.4
Wings	236 ± 59	8 ± 56	6.1 ± 4.9	1.5 ± 1.3	283 ± 26	−5 ± 11	5 ± 18	1.5 ± 3.1
Other	99 ± 42	−177 ± 20	4.2 ± 2.2	0.4 ± 0.3	107 ± 44	−166 ± 21	9.9 ± 2.3	1.1 ± 0.5
NGC 1266								
H$_2$S 1−1 Total	98 ± 5	−18 ± 2	4.2 ± 0.2	0.43 ± 0.02	131 ± 8	19 ± 4	9.9 ± 0.2	1.4 ± 0.1
Core	71 ± 17	−1 ± 5	3.0 ± 1.0	0.22 ± 0.09	71 ± 39	1 ± 10	5.7 ± 5.3	0.4 ± 0.5
Wings	188 ± 84	−1 ± 52	1.4 ± 1.0	0.28 ± 0.24	236 ± 217	−1 ± 247	5.0 ± 8.5	1.3 ± 2.4
Other	118 ± 87	−156 ± 54	−0.7 ± 0.6	−0.09 ± 0.1	140 ± 214	−144 ± 125	−3.2 ± 12.6	−0.5 ± 2.0
H$_2$S 2−2 Core	51 ± 10	−1 ± 4	6.1 ± 1.0	0.33 ± 0.09	59 ± 12	0 ± 5	4.7 ± 0.9	0.29 ± 0.08

Notes. [1]The velocity-integrated flux of the whole line is obtained by integrating the spatially integrated flux of each channel.

Table 4. Brightness temperatures.

Source	$\int T_{b11}dv$ [a] [K km s^{-1}]	$\int T_{b22}dv$ [b] [K km s^{-1}]	$R_{Tb22dv/Tb11dv}$ [c]	T_{b11} [K]	T_{b22} [K]	$R_{Tb22/Tb11}$	Δv [d] [km s^{-1}]
NGC 1377	9.3×10^2	2.4×10^2	0.25	25	7	0.28	65
NGC 4418	3.9×10^3	1.6×10^3	0.40	41	22	0.54	108
NGC 1266	32	40	1.25	3.3	3.7	1.12	56

Notes. This table summarises the values from the observations which are referenced for the RADEX modelling. [a]The velocity-integrated brightness temperatures of H$_2$S $1_{1,0}-1_{0,1}$ transition. [b]The velocity-integrated brightness temperatures of H$_2$S $2_{2,0}-2_{1,1}$ transition. [c]The ratios of (a) to (b). [d]The FWHMs of each line, from a Gaussian fit.
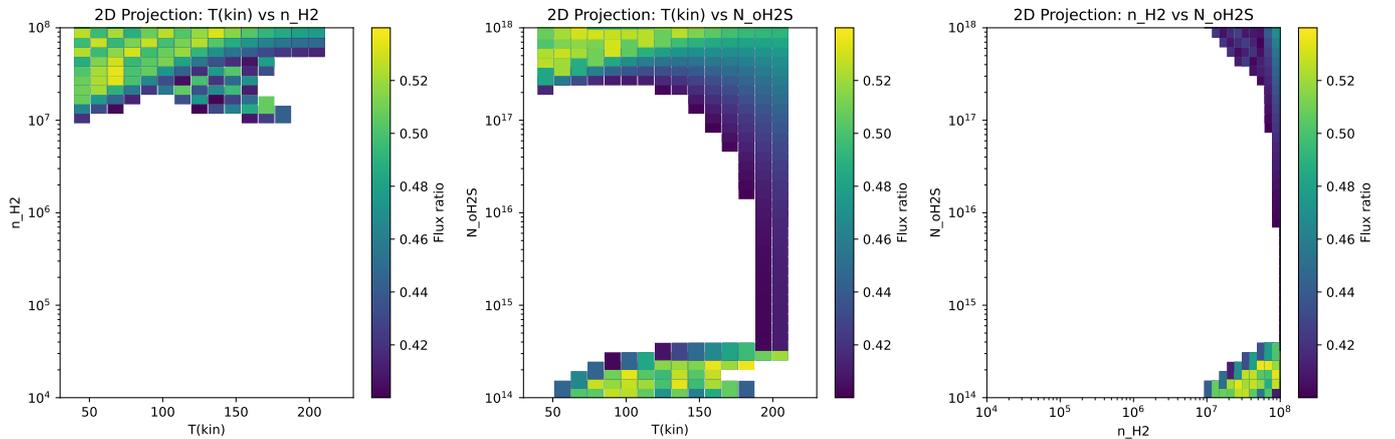

Fig. 9. Result from RADEX modelling for NGC 4418. The line ratio of H$_2$S $2_{2,0}-2_{1,1}$ to H$_2$S $1_{1,0}-1_{0,1}$ (in colour) is plotted in the parameter spaces: *left*: n_{H_2} vs. T_{kin}; *middle*: N_{H_2S} vs. T_{kin}; and *right*: N_{H_2S} vs. n_{H_2}.

has a peak flux of $5.2 \, \text{mJy beam}^{-1}$ ($T_b = 2.4$ K), and the total flux is 5.7 ± 0.2 mJy.

4. Discussions

In a recent study, Sato et al. (2022) presented single-dish observations towards a group of 12 galaxies, revealing the presence of H_2S emission in nine of them. Although the angular resolution of our observations ($\sim 37''$) did not allow us to resolve the emitting region, the lack of correlation between the normalised intensity of the H_2S lines and the presence of observed molecular outflows led us to conclude that the H_2S abundance enhancement does not seem to be directly linked to galactic-scale outflows. Instead, for certain galaxies, including NGC 4418, we proposed that the enhancement could be attributed to radiative processes or small-scale shocks. Additionally, a correlation between H_2S line luminosity and outflow mass hinted at a connection between the dense gas reservoir and the evolution of molecular feedback. The much higher angular-resolution ALMA observations ($0''.1-1''.2$) presented in this work have now provided further insights into the origin of the H_2S in these galaxies. Our new ALMA observations resolve these regions down to scales of $20-30$ pc, revealing compact H_2S emission at galaxy centres. Additionally, some galaxies exhibit relatively broad spectral-line wings, hinting at a connection between the H_2S emission and the presence of a high-velocity outflow. However, a puzzling discrepancy arises: the H_2S-emitting gas appears significantly denser ($10^7-10^8 \, \text{cm}^{-3}$) than the density inferred from CO emission ($\sim 10^5 \, \text{cm}^{-3}$) in NGC 1377 (Sect. 4.3). This difference is worth noting given that the CO-emitting region, from which the density was obtained, is only 2 pc across. It is important to note, though, that the CO emission does not necessarily originate from the same 2 pc region as the H_2S emission. In order to understand the results from our observations and modelling, in the following we consider some likely scenarios for the origin of H_2S emission in these galaxies.

4.1. Possible mechanisms for the formation of gas-phase H_2S

The detection of H_2S in the gas phase implies that one or more mechanisms must exist to release this molecule from dust grains, where it is expected to predominantly form (Charnley 1997; Wakelam et al. 2004; Viti et al. 2004). These mechanisms can enhance the gas-phase abundance of H_2S through several processes. The high density of the gas alone cannot account for the enhanced H_2S abundance, as chemical desorption becomes inefficient at densities above $2 \times 10^4 \, \text{cm}^{-3}$ under dark (high visual extinction) and cold (~ 10 K) conditions (e.g. Vidal et al. 2017; Navarro-Almaida et al. 2020). This suggests that additional processes must be at play to sustain a sufficient amount of gas-phase H_2S for emission.

Radiation from a nuclear starburst or an AGN can lead to the sublimation of volatile species such as H_2S through thermal desorption, efficiently releasing molecules into the gas phase as a result of increased dust temperatures (e.g. Minh et al. 1990; Charnley 1997; Bachiller et al. 2001; Hatchell & Viti 2002; Minh et al. 2007; Woods et al. 2015). Alternatively, in even lower temperature environments, photo-desorption could also contribute to molecule release, particularly if the dust temperature is around $10-50$ K (Goicoechea et al. 2021). Thermal desorption can also be triggered by shocks. The passage of a shock wave through the interstellar medium can compress and heat both the gas and dust, leading to the sublimation of H_2S from grain mantles. If the shock is relatively mild, such as a

C-type shock, it can raise the gas temperature without completely dissociating H_2S molecules (e.g. Pineau-desForets et al. 1993; Holdship et al. 2017). Evidence for the potential role of this mechanism can be provided by the presence of broad line wings in the spectral lines of this molecule.

In regions with high-velocity shocks, direct sputtering may also be a viable mechanism. In this process, energetic particles or ions impact dust grains, physically ejecting H_2S into the gas phase. However, if the shock velocity is too high (e.g. J-type shocks exceeding $\sim 80 \, \text{km s}^{-1}$), it could lead to the complete destruction of H_2S molecules, reducing rather than enhancing their abundance (e.g. Neufeld & Dalgarno 1989).

To better understand the origin of the detected H_2S emission, it is crucial to determine both the kinetic temperature and the density of the gas in the observed regions. These physical conditions will help identify which of the above-mentioned mechanisms is most likely playing a major role in the production of gas-phase H_2S in the sample galaxies. A first hint at the origin of H_2S in the galaxies targeted in this work comes from the gas density derived from our RADEX modelling.

The processes discussed in this section, especially shock-induced desorption, offer a viable explanation for elevated H_2S in galaxy nuclei and may help resolve the puzzling density discrepancy in NGC 1377, which is discussed in Sect. 4.3. While shock-induced desorption is a compelling mechanism to elevate gas-phase H_2S abundances in galaxy centres, it is important to consider the initial solid-phase reservoir of H_2S on dust grains. The presence of H_2S ice typically requires sufficiently low temperatures ($\lesssim 50$ K) for an effective freeze-out (Charnley 1997; Bariosco et al. 2024; Wakelam et al. 2004), conditions that may be uncommon in the warm, dense nuclear regions of luminous infrared galaxies. However, it is plausible that localised cooler regions or episodic shielding within dense clumps or filaments exist, allowing H_2S to accumulate on grain mantles prior to exposure to shocks (Navarro-Almaida et al. 2020; Viti et al. 2004). Alternatively, H_2S ice may have formed earlier in the evolutionary history of the molecular cloud when temperatures were lower, with shocks later releasing this reservoir into the gas phase. These scenarios highlight the necessity of considering the temporal and spatial complexity of physical conditions in galaxy centres to fully understand the high gas-phase H_2S abundances observed.

4.2. Origin of H_2S in the observed galaxies

As mentioned above, we find that a rather high H_2 density of $n_{H_2} > 3 \times 10^6 \, \text{cm}^{-3}$ can adequately reproduce our observational results. In particular, for NGC 4418 and NGC 1266, the implied density is $> 10^7 \, \text{cm}^{-3}$. Our modelling does not allow us to constrain the kinetic temperature within a range of $40-200$ K, nor can the H_2S column density be adequately determined, except for NGC 1266, where the modelling only yields solutions for $N_{H_2S} = 1 \times 10^{14} \, \text{cm}^{-2}$.

A possible explanation for the high values of the density is that the H_2S emission originates from a compact structure within the central region of the galaxy whose size is smaller than that probed by the synthesised beam of our observations ($20-30$ pc). The line profiles provide further clues to the origin of this emission. In particular, the line wings of the H_2S line may trace the base of an outflow. In NGC 1377, for example, the observed density gradient in the outflow (see Fig. 4) is consistent with this scenario. Although Fig. 1a hints at a potential north-south shift in high-velocity gas, the magnitude of this shift is too small, relative to the beam size, to be claimed

confidently. The wing emission could also emerge from unresolved Keplerian rotation close to the SMBH. Notably, higher resolution observations of CO 6−5 in the nucleus of NGC 1377 reveal similar line wings, with dynamics that are not consistent with simple rotation (Aalto et al. 2017). This underscores the need for higher resolution studies to clarify the structure and orientation of the H_2S line wing components.

Alternatively, the observed emission may arise from multiple compact, dense features distributed within the beam, such as shocked gas regions from molecular outflows or dense clumps associated with star formation. Varenius et al. (2014) identified multiple compact radio sources in NGC 4418, each smaller than 8 pc, within a 41 pc region, indicating intense star formation.

We emphasise the presence of line wings in several of the galaxies suggesting a link between the outflow and shocks. We also note the relatively short timescales ($\leq 10^4$ yr) over which H_2S can remain in the gas phase at high density (e.g. Pineau-desForets et al. 1993).

If radiative pumping contributes significantly to excitation, our RADEX-derived densities may be overestimated, since the models assume purely collisional excitation. However, although H_2S can be radiatively pumped at densities exceeding 10^7 cm^{-3}, lower excitation levels of H_2S, such as those in our study, appear to be less affected by this mechanism, as found by Crockett et al. (2014) in Orion KL.

Finally, NGC 4418 presents a particularly intriguing case; the velocity gradient of the H_2S $2_{2,0}-2_{1,1}$ emission appears to align with the large-scale stellar-disc rotation observed by, for example, Wethers et al. (2024), while the H_2S $1_{1,0}-1_{0,1}$ line has an opposite orientation. The inner gas disc has previously been reported to counter-rotate with respect to the stars (e.g. Ohyama et al. 2019; Sakamoto et al. 2021), and the H_2S $1_{1,0}-1_{0,1}$ emission follows this general counter-rotation. However, the nuclear gaseous dynamics is also found to be quite complex with multiple components. Redshifted absorption structures are, for example, suggested to indicate an inflow of gas to the central region (e.g. González-Alfonso et al. 2012; Costagliola et al. 2013; Sakamoto et al. 2013). The H_2S $1_{1,0}-1_{0,1}$ emission shows a redshifted extension on the blue side of the nuclear rotation (Fig. 5), which may signify gas inflowing in the disc, or a bar. However, this extension has the same orientation as the larger scale redshifted outflow found by Wethers et al. (2024) with MUSE. Furthermore, Sakamoto et al. (2021) discussed the possibility that a redshifted absorption could be caused by a slanted outflow that is not parallel to the minor axis of the disc. The high-velocity components of H_2S $1_{1,0}-1_{0,1}$ show slightly extended emission along the minor axis of the disc (redshifted emission towards the north-west and blueshifted emission towards the south-east; Fig. 5a). Future, higher resolution observations are critical to determine if the redshifted H_2S $1_{1,0}-1_{0,1}$ emission is due to inflowing gas or a tilted outflow.

Why the H_2S $1_{1,0}-1_{0,1}$ and $2_{2,0}-2_{1,1}$ emission appear not to follow the same orientation is unclear, but it may be caused by excitation effects in the complex nuclear dynamics. Furthermore, the blueshifted wing of the H_2S $2_{2,0}-2_{1,1}$ line is blended with other spectral features (see Fig. 6), making it difficult to derive a clear velocity gradient.

4.3. Why CO and H_2S yield different densities

Interestingly, as mentioned above, the density derived from the CO observations within a compact region of 2 pc in NGC 1377 is only $\sim 10^5$ cm^{-3}, which is significantly smaller than the density

derived from the H_2S. Obtaining different densities as derived from H_2S and CO observations is not uncommon. For example, Bouvier et al. (2024) find a gas temperature of $30-159$ K and $n_{gas} \geq 10^7$ cm^{-3} at the inner circum-molecular zone (CMZ) of NGC 253, while from CO observations, the implied density is 10^{3-4} cm^{-3} (Tanaka et al. 2024). This difference has also been observed in other astrophysical environments, such as evolved stars. Gold et al. (2024) recently reported the first detection of H_2S in the planetary nebula M1-59. These authors, in line with our approach, used RADEX modelling and found densities for H_2S greater than 10^7 cm^{-3}, while the CO-derived densities were around 10^4 cm^{-3}. Additionally, in another galactic example, ALMA observations of the evolved star W43A (Tafoya et al. 2020) revealed that CO emission traces a collimated bipolar outflow, surrounded by higher density material traced by dust and H_2S. The gas density associated with H_2S in this star is estimated to be around 10^8 cm^{-3}, which is similar to the values for the galaxies in our study.

In all the cases mentioned above, the sources are known to have high-velocity outflows and/or shocks associated. In the case of NGC 253, Bouvier et al. (2024) concluded that there is strong evidence indicating that H_2S is tracing shocks. For the galactic sources M1-59 and W43A, they are known to exhibit high-velocity collimated outflows and shocks. Therefore, H_2S emission seems to be associated with shocks in a wide variety of astrophysical phenomena. As mentioned above, our ALMA observations reveal the presence of relatively broad spectral line wings. This strongly suggests that the presence of H_2S in these galaxies could also be related to an outflow that compresses gas into compact high-density regions. Particularly, in the case of NGC 1377, the enhancement of H_2S abundance could be associated with shocks, which are potentially created by the collimated outflow that has been observed in CO (Fig. 3, and Aalto et al. 2020). In this scenario, CO would be tracing lower density gas, potentially in an accretion disc and/or the base of a high-velocity outflow, whereas H_2S would be tracing a higher density region. This region traced by H_2S could be also the densest parts of the gas in a clumpy torus around the nucleus.

It is important to note that while high-velocity gas is observed, the velocity experienced locally by the shocked gas may be lower than the bulk outflow speed. Indeed, molecules such as H_2S would be dissociated in the passage of fast shocks exceeding ~ 50 km s^{-1} (Neufeld & Dalgarno 1989). However, if sputtering induced by shocks is the dominant process releasing H_2S into the gas phase, as proposed by Bouvier et al. (2024), this implies that gas and dust grains were already moving at significant velocities relatively to their ambient medium before the shock impact. Consequently, the relative velocity between the gas and the shock front could be moderate enough to prevent complete molecular dissociation, thereby allowing H_2S to survive and be detected. In this scenario, H_2S traces denser regions where shocks act to liberate molecules without fully destroying them, even in environments with otherwise high-velocity outflows. This interpretation aligns with the studies of NGC 1266, where Pellegrini et al. (2013), Otter et al. (2024) found that shocks are likely slow C types (~ 30 km s^{-1}), which is consistent with conditions that preserve molecules such as H_2S while still enabling their release from the ice mantles around dust grains.

5. Conclusions

In this paper, we present high-angular-resolution ALMA observations of H_2S emission in a sample of nearby galaxies,

providing new insights into the origin and excitation conditions of this molecule in extragalactic environments.

Our main conclusions are as follows:

- H_2S emission is detected from centrally compact regions ($\lesssim 100-150$ pc) in all observed galaxies, with some sources showing broad spectral-line wings, indicative of kinematic components related to outflows or shocks. In NGC 4418, H_2S also appears to be tracing gas that is counter-rotating. A peculiar redshifted emission feature may be inflowing gas, or possibly a slanted outflow.

- RADEX modelling suggests that the H_2S-emitting gas is characterised by high densities, with $n_{H_2} \gtrsim 10^7$ cm^{-3} in NGC 4418 and NGC 1266, and $n_{H_2} > 3 \times 10^6$ cm^{-3} in NGC 1377. The derived densities are significantly higher than those inferred from CO observations, suggesting that H_2S traces a denser gas component.

- The high-density H_2S-emitting gas may originate from compact structures within the nuclear region, such as dense clumps, accretion flows onto a supermassive black hole, or shocked regions driven by molecular outflows.

- The presence of broad wings in the H_2S spectral profiles, combined with the detection of collimated CO outflows in some galaxies, supports a scenario where shocks associated with outflows contribute to the release of H_2S into the gas phase, likely via sputtering or thermal desorption from dust grains.

- Although high-velocity gas is present, the relative velocity of gas with respect to the shock front may be lower, preventing the complete dissociation of H_2S molecules even in fast outflows, as proposed in earlier studies (e.g. Bouvier et al. 2024; Neufeld & Dalgarno 1989).

- We also note important caveats related to the RADEX modelling, such as uncertainties introduced by assumptions about source size, the ortho-to-para ratio of H_2S, and the use of scaled collisional rates. These factors should be carefully considered when interpreting the derived physical conditions.

Overall, our results suggest that H_2S is a valuable tracer of dense, shocked gas in galactic nuclei and outflows, and further multi-line studies at higher spatial resolution will be crucial to fully characterise its role in feedback processes and molecular chemistry in active galaxies.

References

Aalto, S. 2012, Proc. IAU, 8, 199
Aalto, S., Muller, S., Sakamoto, K., et al. 2012a, A&A, 546, A68
Aalto, S., Garcia-Burillo, S., Muller, S., et al. 2012b, A&A, 537, A44
Aalto, S., Garcia-Burillo, S., Muller, S., et al. 2015, A&A, 574, A85
Aalto, S., Costagliola, F., Muller, S., et al. 2016, A&A, 590, A73
Aalto, S., Muller, S., Costagliola, F., et al. 2017, A&A, 608, A22
Aalto, S., Falstad, N., Muller, S., et al. 2020, A&A, 640, A104
Alatalo, K. 2015, ApJ, 801, L17
Alatalo, K., Blitz, L., Young, L. M., et al. 2011, ApJ, 735, 88
Bachiller, R., Pérez Gutiérrez, M., Kumar, M. S., & Tafalla, M. 2001, A&A, 372, 899
Barcos-Muñoz, L., Aalto, S., Thompson, T. A., et al. 2018, ApJ, 853, L28
Bariosco, V., Pantaleone, S., Ceccarelli, C., et al. 2024, MNRAS, 531, 1371
Baryshev, A. M., Hesper, R., Mena, F. P., et al. 2015, A&A, 577, A129
Belitsky, V., Lapkin, I., Fredrixon, M., et al. 2018, A&A, 612, A23
Bouvier, M., Viti, S., Behrens, E., et al. 2024, A&A, 689, A64
Charnley, S. B. 1997, ApJ, 481, 396
Chung, A., Yun, M. S., Narayanan, G., Heyer, M., & Erickson, N. R. 2011, ApJ, 732, L15
Cicone, C., Maiolino, R., Sturm, E., et al. 2014, A&A, 562, A21
Cicone, C., Maiolino, R., Aalto, S., Muller, S., & Feruglio, C. 2020, A&A, 633, A163
Costagliola, F., Aalto, S., Sakamoto, K., et al. 2013, A&A, 556, A66
Costagliola, F., Sakamoto, K., Muller, S., et al. 2015, A&A, 582, A91
Crockett, N. R., Bergin, E. A., Neill, J. L., et al. 2014, ApJ, 781, 114
Daniel, F., Dubernet, M. L., Pacaud, F., & Grosjean, A. 2010, A&A, 517, A13
Daniel, F., Dubernet, M. L., & Grosjean, A. 2011, A&A, 536, A76
Dasyra, K. M., Combes, F., Oosterloo, T., et al. 2016, A&A, 595, L7
Davis, T. A., Krajnović, D., McDermid, R. M., et al. 2012, MNRAS, 426, 1574
Draine, B. T., & McKee, C. F. 1993, ARA&A, 31, 373
Dubernet, M. L., Daniel, F., Grosjean, A., et al. 2006, A&A, 460, 323
Dubernet, M. L., Daniel, F., Grosjean, A., & Lin, C. Y. 2009, A&A, 497, 911
Ediss, G. A., Carter, M., Cheng, J., et al. 2004, Proceedings of the Fifteenth International Symposium on Space Terahertz Technology, 181
Falstad, N., Hallqvist, F., Aalto, S., et al. 2019, A&A, 623, A29
Falstad, N., Aalto, S., König, S., et al. 2021, A&A, 649, A105
Ferrara, A., & Scannapieco, E. 2016, ApJ, 833, 46
Feruglio, C., Daddi, E., Fiore, F., et al. 2011, ApJ, 729, L4
Fluetsch, A., Maiolino, R., Carniani, S., et al. 2019, MNRAS, 483, 4586
Fontani, F., Roueff, E., Colzi, L., & Caselli, P. 2023, A&A, 680, A58
Gao, Y., & Solomon, P. M. 2004, ApJ, 606, 271
García-Burillo, S., Combes, F., Usero, A., et al. 2015, A&A, 580, A35
Goicoechea, J. R., Aguado, A., Cuadrado, S., et al. 2021, A&A, 647, A10
Gold, K. R., Schmidt, D. R., & Ziurys, L. M. 2024, ApJ, 976, 196
González-Alfonso, E., Fischer, J., Graciá-Carpio, J., et al. 2012, A&A, 541, A4
Harada, N., Sakamoto, K., Martín, S., et al. 2018, ApJ, 855, 49
Hatchell, J., & Viti, S. 2002, A&A, 381, L33
Holdship, J., Viti, S., Makrymallis, A., & Priestley, F. 2017, AJ, 154, 38
Imanishi, M. 2006, AJ, 131, 2406
Iono, D., Wilson, C. D., Yun, M. S., et al. 2009, ApJ, 695, 1537
Lutz, D., Sturm, E., Janssen, A., et al. 2020, A&A, 633, A134
Maiolino, R., Russell, H. R., Fabian, A. C., et al. 2017, Nature, 544, 202
Martinez, N. C., Paron, S., Ortega, M. E., et al. 2024, A&A, 692, A97
Matsushita, S., Trung, D.-V., Boone, F., et al. 2015, JKAS, 30, 439
Mifsud, D. V., Kaňuchová, Z., Herczku, P., et al. 2021, Space Sci. Rev., 217, 14
Minh, Y. C., Irvine, W. M., McGonagle, D., & Ziurys, L. M. 1990, ApJ, 360, 136
Minh, Y. C., Muller, S., Liu, S.-Y., & Yoon, T. S. 2007, ApJ, 661, L135
Mitchell, G. F. 1984, ApJ, 287, 665
Morganti, R., Oosterloo, T., Raymond Oonk, J. B., Frieswijk, W., & Tadhunter, C. 2015, A&A, 580, A1
Navarro-Almaida, D., Gal, R. L., Fuente, A., et al. 2020, A&A, 637, A39
Neufeld, D. A., & Dalgarno, A. 1989, ApJ, 340, 869
Nishimura, Y., Watanabe, Y., Harada, N., et al. 2017, ApJ, 848, 17
Nyland, K., Alatalo, K., Wrobel, J. M., et al. 2013, ApJ, 779, 173
Ohyama, Y., Sakamoto, K., Aalto, S., & Gallagher, J. S. 2019, ApJ, 871, 191
Otter, J. A., Alatalo, K., Rowlands, K., et al. 2024, ApJ, 975, 142
Pellegrini, E. W., Smith, J. D., Wolfire, M. G., et al. 2013, ApJ, 779, L19
Pereira-Santaella, M., Colina, L., García-Burillo, S., et al. 2018, A&A, 616, A171
Pineau-desForets, G., Roueff, E., Schilke, P., & Flower, D. R. 1993, MNRAS, 262, 915
Privon, G. C., Herrero-Illana, R., Evans, A. S., et al. 2015, ApJ, 814, 39
Roussel, H., Helou, G., Beck, R., et al. 2003, ApJ, 593, 733
Roussel, H., Helou, G., Smith, J. D., et al. 2006, ApJ, 646, 841
Saito, T., Takano, S., Harada, N., et al. 2022, ApJ, 935, 155
Sakamoto, K., Aalto, S., Costagliola, F., et al. 2013, ApJ, 764, 42
Sakamoto, K., Aalto, S., Combes, F., Evans, A., & Peck, A. 2014, ApJ, 797, 90
Sakamoto, K., Aalto, S., Barcos-Muñoz, L., et al. 2017, ApJ, 849, 14
Sakamoto, K., Martin, S., Wilner, D. J., et al. 2021, ApJ, 923, 240
Sanders, D. B., & Mirabel, I. F. 1996, ARA&A, 34, 749
Sanders, D. B., Mazzarella, J. M., Kim, D.-C., Surace, J. A., & Soifer, B. T. 2003,

AJ, 126, 1607
Sato, M. T., Aalto, S., Kohno, K., et al. 2022, A&A, 660, A82
Spoon, H. W. W., Marshall, J. A., Houck, J. R., et al. 2006, ApJ, 654, L49
Sturm, E., Gonzlez-Alfonso, E., Veilleux, S., et al. 2011, ApJ, 733, L16
Tafoya, D., Imai, H., Gómez, J. F., et al. 2020, ApJ, 890, L14
Tanaka, K., Mangum, J. G., Viti, S., et al. 2024, ApJ, 961, 18
Van der Tak, F. F., Boonman, A. M., Braakman, R., & Van Dishoeck, E. F. 2003, A&A, 412, 133
Van Der Tak, F. F., Black, J. H., Schöier, F. L., Jansen, D. J., & Van Dishoeck, E. F. 2007, A&A, 468, 627

Varenius, E., Conway, J. E., Martí-Vidal, I., et al. 2014, A&A, 566, A15
Veilleux, S., Meléndez, M., Sturm, E., et al. 2013, ApJ, 776, 27
Veilleux, S., Maiolino, R., Bolatto, A. D., & Aalto, S. 2020, A&ARv, 28, 2
Vidal, T. H. G., Loison, J.-C., Jaziri, A. Y., et al. 2017, MNRAS, 469, 435
Viti, S., Collings, M. P., Dever, J. W., McCoustra, M. R., & Williams, D. A. 2004, MNRAS, 354, 1141
Wakelam, V., Castets, A., Ceccarelli, C., et al. 2004, A&A, 413, 609
Walter, F., Bolatto, A. D., Leroy, A. K., et al. 2017, ApJ, 835, 265
Wethers, C. F., Aalto, S., Privon, G. C., et al. 2024, A&A, 683, A27
Woods, P. M., Occhiogrosso, A., Viti, S., et al. 2015, MNRAS, 450, 1256